Appl Phys A
DOI 10.1007/s00339-012-6956-9

Applied Physics A
Materials Science & Processing

Structural investigations of silicon nanostructures grown by self-organized island formation for photovoltaic applications

Maurizio Roczen · Martin Schade · Enno Malguth · Gordon Callsen · Thomas Barthel · Orman Gref · Jan A. Töfflinger · Andreas Schöpke · Manfred Schmidt · Hartmut S. Leipner · Florian Ruske · Matthew R. Phillips · Axel Hoffmann · Lars Korte · Bernd Rech

Received: 14 April 2012 / Accepted: 19 April 2012

Abstract The self-organized growth of crystalline silicon nanodots and their structural characteristics are investigated. For the nanodot synthesis, thin amorphous silicon (a-Si) layers with different thicknesses have been deposited onto the ultrathin (2 nm) oxidized (111) surface of Si wafers by electron beam evaporation under ultrahigh vacuum conditions. The solid phase crystallization of the initial layer is induced by a subsequent in situ annealing step at 700 °C, which leads to the dewetting of the initial a-Si layer. This process results in the self-organized formation of highly crystalline Si nanodot islands. Scanning electron microscopy confirms that size, shape, and planar distribution of the nanodots depend on the thickness of the initial a-Si layer. Cross-sectional investigations reveal a single-crystalline structure of the nanodots. This characteristic is observed as long as the thickness of the initial a-Si layer remains under a certain threshold triggering coalescence. The underlying ultra-thin oxide is not structurally affected by the dewetting process. Furthermore, a method for the fabrication of close-packed stacks of nanodots is presented, in which each nanodot is covered by a 2 nm thick SiO_2 shell. The chemical composition of these ensembles exhibits an abrupt Si/SiO_2 interface with a low amount of suboxides. A minority charge carrier lifetime of 18 μs inside of the nanodots is determined.

1 Introduction

The synthesis of Si nanodot structures within a SiO_2 matrix is currently of high interest for 3rd generation solar cell applications [1–4]. Such low dimensional structures exhibit the potential to exceed the Shockley–Queisser efficiency limit [5] by exploiting quantum size effects (QSE) [6]. The QSE predicts the possibility of size dependent band gap engineering for nanodot diameters less than 5 nm [7].

Conceivable applications of QSE in a solar cell device may not only exist as a nanodot absorber with a tunable band gap [8], but also as nanodot heteroemitter with energy selective contacts [9]. Such a "hot carrier cell" can achieve conversion efficiencies above 50 % by extracting charge carriers at high excitation energies before thermal relaxation can occur [10].

The SiO_2 matrix plays an important role in minimizing the recombination of charge carriers: on the one hand, it passivates dangling bonds at the Si/SiO_2 interface [11], on the other hand, it reduces the leakage current of majority charge carriers due to the additional SiO_2 barriers [12]. Therefore, high open circuit voltages are expected even without exploiting QSE [13].

However, several requirements on the nanodot heteroemitter must be fulfilled for the implementation in a solar

The first two authors contributed equally to this work.

M. Roczen (✉) · E. Malguth · T. Barthel · O. Gref · J.A. Töfflinger · A. Schöpke · M. Schmidt · F. Ruske · L. Korte · B. Rech
Helmholtz-Zentrum Berlin, Institute for Silicon Photovoltaics, Kekuléstrasse 5, 12489 Berlin, Germany
e-mail: Maurizio.Roczen@helmholtz-berlin.de
Fax: +49-30-806241333

M. Schade · H.S. Leipner
Interdisziplinäres Zentrum für Materialwissenschaften, Martin-Luther-Universität Halle-Wittenberg, Heinrich-Damerow-Str. 4, 06120 Halle, Germany

G. Callsen · A. Hoffmann
Institut für Festkörperphysik, Technische Universität Berlin, Hardenbergstrasse 36, 10623 Berlin, Germany

M.R. Phillips
Department of Physics and Advanced Materials, University of Technology Sydney, PO Box 123, Broadway, NSW 2007, Australia

Published online: 09 May 2012

cell device: (i) doping of nanodots is required in order to induce a band bending in the absorber, (ii) charge carrier transport across the oxide separating nanodots needs to be achieved by implementing an oxide thickness $\leq$2 nm [14], and (iii) the absorber needs to be passivated.

Recent approaches to meet these requirements are based on the decomposition and subsequent crystallization of substoichiometric SiO_x ($0 < x < 2$) films at temperatures exceeding 1100 °C [15–17]. Although a good control over both, the nanodot size and the nanodot density has been achieved, an efficient carrier extraction from the nanodots through the SiO_2 barrier is still an issue.

The self-organized island growth of intrinsic silicon nanodots based on a solid phase crystallization (SPC) mechanism [18] allows the formation of highly crystalline and close packed Si nanostructures from 600 °C [19]. The synthesis is performed under ultrahigh vacuum (UHV) conditions by depositing firstly a thin amorphous silicon (a-Si) layer on top of the oxidized surface of a crystalline silicon (c-Si) wafer. During a subsequent thermal treatment, the energetically unfavorable interface energy between the crystallizing Si layer and the underlying SiO_2 causes the growth of isolated nanodot islands in order to minimize the free energy of the system [20, 21].

Although the dewetting process of Si [22–25] on top of a thick (>100 nm) insulating layer is well known in literature, most structural investigations were performed by means of scanning electron microscopy (SEM) or atomic force microscopy. Thus, only little information was obtained on the crystalline structure of such Si nanodots and its dependence on the nanodot size. Furthermore, the dewetting of a-Si on top of an ultra-thin oxide layer and the potential of the nanodots for the implementation in a solar cell device are poorly investigated at best.

In this contribution, we present a systematic study on the self-organized island growth of nanodot structures on top of ultrathin tunneling oxides (2 nm) by utilizing intrinsic a-Si layers. The structural properties of the c-Si nanodots are investigated by analytical electron microscopy and Raman spectroscopy. The chemical composition of the SiO_2 matrix and its passivation quality for the silicon nanodots are presented. Furthermore, the dependence of the nanodot size, shape, density, and crystalline structure on the initial layer thickness is investigated. Finally, several layers of close packed nanodots are fabricated in order to evaluate the implementation of the nanostructures as a heteroemitter in a solar cell device.

2 Experimental details

2.1 Sample preparation

Boron doped float zone c-Si (111) wafers with a resistivity of 1–5 Ω cm were used as substrates for nanodot synthesis. The Si wafers were cleaned by the standard RCA process followed by etching in 1 % hydrofluoric acid solution. This results in a nonoxidized, hydrogen terminated Si:H 1×1 surface with a roughness of around 0.6 nm which impedes an oxide formation for a few minutes [26]. After immediate transfer into the UHV chamber (base pressure $<5 \times 10^{-9}$ mbar), the wafers were heated up to 1000 °C in order to desorb hydrogen and other residual contaminations from the surface. At this temperature, the 7×7 reconstruction of the wafer surface is induced, as confirmed by in situ reflection high energy electron diffraction analysis. This careful pretreatment guarantees a well defined and reproducible surface for the following steps.

A controlled layer by layer oxidation (plasma oxidation) of the wafer surface was performed at a pressure of 2×10^{-6} mbar by neutral atomic oxygen atoms with thermal impact energies ($E_{\mathrm{kin}} < 1$ eV), which were provided by a radio frequency plasma cracker source (RF-PCS, Oxford Scientific/Specs) [27]. The resulting 2 nm thick plasma oxide provides an abrupt Si/SiO_2 interface with a low density of interfacial defect states [28]. A tunneling current through the as-prepared oxide barrier has already been demonstrated successfully in a previous publication [19].

Afterward, thin a-Si films with thicknesses between 1–20 nm were deposited at a pressure of 10^{-8} mbar onto such oxidized wafers by electron beam evaporation of intrinsic Si targets. Both the deposition rate of 1 Å/s and the film thickness were monitored by a quartz crystal microbalance. The substrate was kept at room temperature during the deposition. The solid phase crystallization of the a-Si films was achieved by in situ annealing at 700 °C for 5 minutes. During the crystallization process the dewetting of the initial layer occurs, resulting in the formation of nanosized Si droplets. Experiments have shown that the dewetting of the intrinsic a-Si layers could also be performed at 600 °C, but it would need at least 30 min for completion in this case. By repeating the plasma oxidation, the a-Si layer deposition and the crystallization process, several stacks of nanodots were grown. Each nanodot is then covered by an ultrathin SiO_2 shell.

In addition, Si nanodots were also grown onto quartz glass substrates (Suprasil, Heraeus) in order to perform investigations by Raman spectroscopy. The glass substrates were cleaned by immersing them in a piranha etch (H_2SO_4/H_2O_2) solution at 120 °C. For nanodot synthesis, the same process steps as for the c-Si wafers were performed except for the initial plasma oxidation.

2.2 Characterization

In situ XPS measurements using X-rays with a photon energy of 1253.6 eV provided by a Mg-K_α source have been carried out in order to investigate the chemical composition

of the Si/SiO_2 interface. A quantitative analysis of the chemical shift of the Si 2p oxidation levels, Si^{j+} ($j = 0$–4) provides information on the chemical bonds of the Si atoms, and hence the stoichiometry of the interface [29].

The samples were also inspected by ex-situ scanning electron microscopy (SEM) utilizing a Philips XL 30 FE-SEM. The acceleration voltage was set to 12 kV. For high-resolution (HRSEM) imaging of the nanodot samples, we applied a Zeiss Supra 55VP FESEM equipped with an in-lens secondary electron detector. In addition, the morphology of the nanodots was investigated by μ-Raman spectroscopy using an Olympus BX 40 microscope system equipped with an Ar^+ ion laser operating at a wavelength of 457.9 nm.

To evaluate the quality of the passivation of the nanodots by the SiO_2 matrix time resolved photoluminescence (TRPL) spectroscopy was performed. It allows the determination of the lifetime of photogenerated charge carriers inside of the nanodots. The samples were excited with a pulsed dye laser providing excitation wavelengths of 337 nm and 743 nm. The pulse length was 3 ns. The PL signal was detected by a silicon avalanche photodiode after dispersion in a prism monochromator.

Finally, electron transparent cross-section samples have been prepared by applying standard transmission electron microscopy (TEM) preparation including mechanical grinding, polishing, dimpling, and Ar^+ ion milling. High-resolution transmission electron microscopy (HRTEM) investigations were carried out using a JEM 4010 transmission electron microscope at an acceleration voltage of 400 kV. In addition, electron energy loss spectroscopy (EELS) was applied in order to obtain compositional information. For this purpose, a dedicated VG HB 501 UX scanning transmission electron microscope equipped with a Gatan ENFINA 1000 parallel electron energy loss spectrometer was used. This instrument was operated at an accelerating voltage of 100 kV during the EELS measurements.

3 Results and discussion

3.1 Nanodot formation by annealing intrinsic a-Si films

Since the average size of the silicon nanodots is governed by the initial a-Si film thickness [19], three different thicknesses d (20 nm, 3 nm, and 1 nm) have been chosen for the initial a-Si film to perform structural characterizations. By acquiring SEM images of the films after the annealing at 700 °C, an overview of size, shape, and density of the nanodots was established. SEM images acquired under an angle of 60° to the surface are presented in Fig. 1a ($d = 20$ nm), Fig. 1b ($d = 3$ nm), and Fig. 1d (stack). The image in Fig. 1c ($d = 1$ nm) as well as the insets were acquired under an angle of 90° to the surface.

The nanodots displayed in Fig. 1a are round and well separated and exhibit diameters of 50–80 nm. However, many

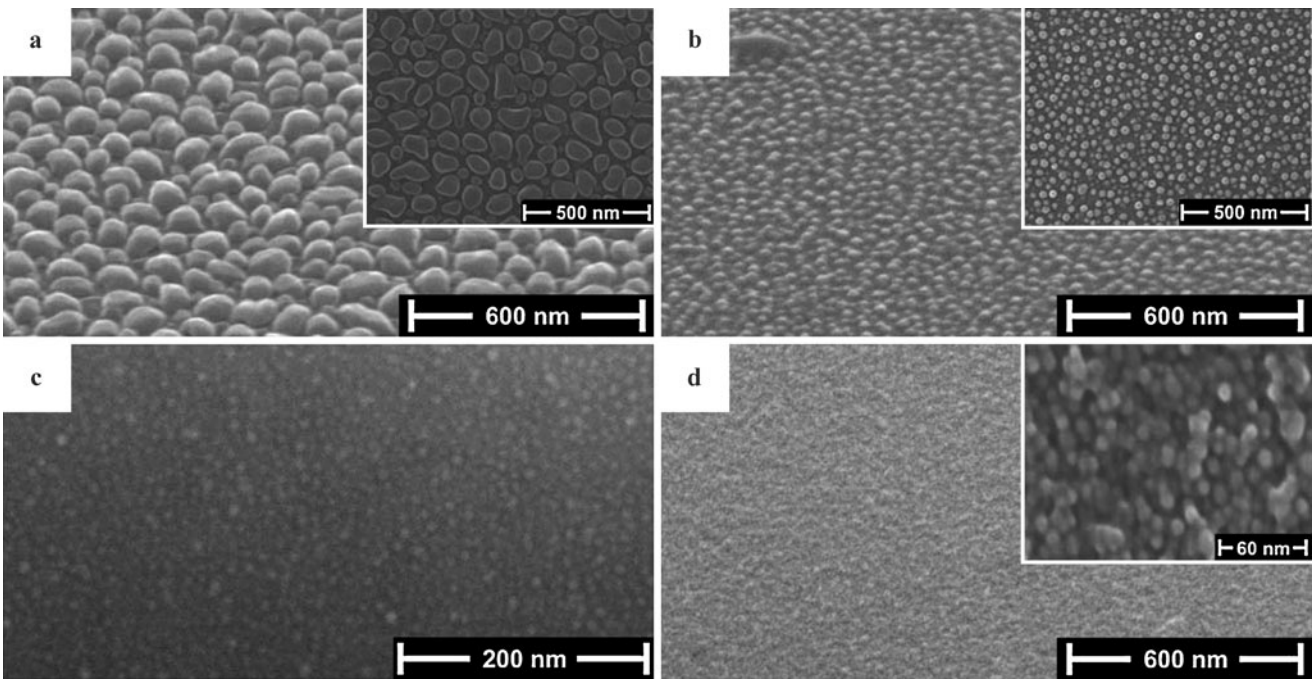

Fig. 1 SEM and HRSEM images (secondary electron contrast) of annealed intrinsic a-Si films with different initial film thicknesses: (**a**) 20 nm Si, (**b**) 3 nm Si, (**c**) 1 nm Si (HRSEM), and (**d**) a stack of 8 nanodot layers, each with initial Si layer thickness of 2 nm and separated by a 2 nm plasma oxide

oval and elongated structures are also visible. In contrast, the dewetting of a 3 nm a-Si layer (Fig. 1b) results in a higher areal nanodot density with much smaller, mainly spherical nanodots having an average diameter of 15 nm. The areal density of nanodots is further increased after dewetting the 1 nm a-Si layer as shown in Fig. 1c, which yields nanodot diameters of 7–10 nm.

To determine the crystalline fraction of the nanodots, the Raman spectrum of Si nanodots with an average diameter of 60 nm grown on a quartz substrate was acquired. Because of the small scattering volume of the nanodots, the major part of the signal can be attributed to the substrate. Hence, the Raman spectra of both, the pure quartz substrate and a c-Si wafer were acquired as reference, also. Finally, the Raman spectrum of the quartz substrate was subtracted from the measured Raman spectrum of the nanodot sample to obtain the pure nanodot spectrum. All spectra are presented in Fig. 2.

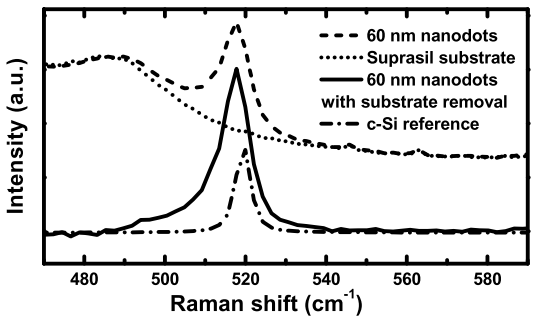

Fig. 2 Raman spectra of Si nanodots deposited on Suprasil glass, of the uncoated Suprasil substrate and of a c-Si wafer. The signal of pure Suprasil glass was subtracted from the nanodot sample in order to compare the Raman spectrum of the nanodots with the Raman spectrum of crystalline Si

The background subtracted Raman spectrum of the nanodots (solid line) exhibits a peak located at 518 cm^{-1} with a full width at half maximum of 8 cm^{-1} which can be attributed to the TO phonon mode of crystalline silicon [30]. The corresponding peak is red shifted by 2 cm^{-1} and broadened by 4 cm^{-1} compared to the related peak in the Raman spectrum of the c-Si reference. These deviations can be attributed to tensile stress [31], which may exist due to the occurrence of lattice mismatch at the Si/SiO_2 surfaces. However, no contribution of the TO phonon mode of amorphous silicon is observed which would appear as a broad peak located at 480 cm^{-1} [32]. By fitting the spectrum with 3 Gaussian peaks, a crystalline fraction of almost 100 % was calculated [33]. In summary, the Raman investigations indicate that the whole initial a-Si film was transformed into crystalline nanodots by the dewetting process.

To confirm these findings and to investigate the internal structure of single nanodots, HRTEM was performed on nanodots with various sizes. Figure 3 shows two HRTEM micrographs of cross section samples resulting from the annealing of a 20 nm thick a-Si film (Fig. 3a) and a 3 nm a-Si film (Fig. 3b), respectively. Single Si nanodots and their close surroundings are visible. In the lower part, the single-crystalline Si (111) substrate is visible. On top of the substrate, the 2 nm thick SiO_2 layer (confirmed by EELS) is visible. The HRTEM micrographs reveal that it is atomically

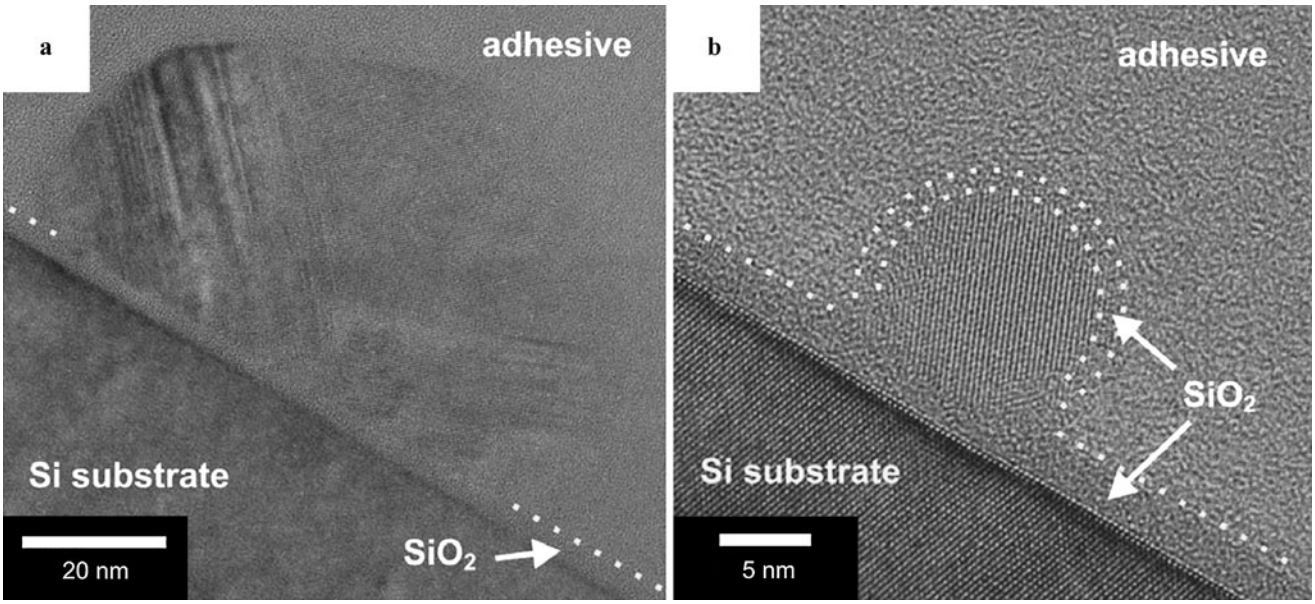

Fig. 3 HRTEM micrographs showing cross-sections of single nanodots emerged after the annealing of intrinsic Si films with an as-deposited film thickness of (**a**) 20 nm and (**b**) 3 nm. White guide lines are drawn to mark the upper border of the plasma oxide in both figures and the native oxide shell of the nanodot in (**b**)

flat as to be expected. The nanodots are situated on top of the oxide and are surrounded by a 1 nm thick oxide shell, which originates from native oxidation due to the long exposure to air prior to the HRTEM analysis [34]. The whole structure is embedded in an adhesive utilized for classic TEM cross-section preparation. Since the adhesive and the SiO_2 exhibit a slightly different contrast in the HRTEM micrographs, a distinction between them is possible. In addition, no remaining a-Si or c-Si layer on top of the plasma oxide could be found besides the nanodots, confirming the complete dewetting of the initial a-Si layer.

Both Figs. 3a and 3b demonstrate that the nanodot structure penetrates a few angstrom into the underlying oxide, but without penetrating into the substrate. Comparing the density of states in the Si band gap at the c-Si wafer/SiO_2 interface (D_{it}) of a plasma oxidized wafer before and after the nanodot formation, only a slight increase in the D_{it} is measured after nanodot growth [35]. This means that during nanodot growth the c-Si wafer/SiO_2 interface remains structurally unaffected, and hence the passivation quality of the plasma oxide is maintained.

The nanodot in Fig. 3a exhibits a hemispherical geometry with a lateral and medial size of 85 nm and 45 nm, respectively, which corresponds to the estimations made for the nanodots in Fig. 1a. Its polycrystalline structure exhibits domains of different crystalline orientations. No correlation with the crystallographic orientation of the substrate is observed. The top part of the nanodot exhibits an undisturbed periodic structure whereas stacking faults are visible at the right and left hand side. No clearly crystalline structure is visible at the border of the nanodot in the vicinity to the oxide layer. However, these areas might also be crystalline but appear amorphous in the HRTEM micrographs due to an unfavorable orientation of the crystallites. Furthermore, EELS measurements show no evidence of silicon oxide inside of the nanodots.

Compared to the nanodot in Fig. 3a, the nanodot in Fig. 3b has a more spherical shape with a diameter of about 12 nm and a smaller contact angle in respect to the substrate. It has a single-crystalline structure being different from the crystal orientation of the Si substrate. Some lattice perturbations are visible at the border of the nanodot. Amorphous areas appear again only close to the silicon oxide layer.

Although dewetting took place after annealing a 1 nm a-Si layer, HRTEM micrographs (not shown) exhibit only a rough amorphous layer of 4 nm height on top of the Si wafer. No difference in contrast to the plasma oxide is observed. Since the plasma oxide is atomically flat, as can be seen in Fig. 3, it is supposed that the nanodots are completely oxidized due to exposure to air. The complete oxidation would explain both the irregular shape of the layer and its thickness, being the sum of the oxide layer and the oxidized nanodots.

The observations show that with increasing initial layer thickness and, therefore, nanodot size, the morphology of the nanostructures becomes more polycrystalline. A possible explanation is given by considering the coalescence of small single-crystalline nanodots to larger polycrystalline structures. This would also explain the elongated shape of larger nanodots as shown in Fig. 1a and the top view image in the inset. In this case, an initial a-Si layer thickness threshold exists (between 3 nm and 20 nm), which triggers the coalescence during the dewetting process.

3.2 Stack of intrinsic Si nanodot layers

In order to evaluate the application of the nanostructures as a heteroemitter in a solar cell device, several layers of close packed nanodots were grown by repeating the nanodot formation cycle (i.e., plasma oxidation, intrinsic a-Si deposition, annealing).

Figure 1d shows the SEM images of a multiple nanodot system in which the cycle was performed for 8 times and finalized by a plasma oxidation step of the uppermost nanodots. The thickness of each deposited a-Si layer was 2 nm. The density of the nanodots at the surface is much higher compared to a single nanodot layer of comparable initial layer thickness (Fig. 1b). This can be explained by the occupation of inter-nanodot regions by the following nanodot layers as appears in the top view SEM image in the inset of Fig. 1d.

Figure 4 illustrates a cross sectional HRTEM micrograph of the same sample. The substrate is located at the top part of the image, followed by the substrate passivation plasma oxide. A high density of spherical, single-crystalline Si nanodots is visible having random crystal orientations. The diameter of the nanodots is 8–10 nm and they are stacked upon each other with an overall stack height of 40 nm. The plasma oxide separating each nanodot cannot be seen since the HRTEM micrographs represent only a 2D projection of the sample. However, a nanodots separating oxide layer of 2 nm thickness is assumed since the oxidation of the nanodots is performed in the same manner as the plasma oxidation of the substrate surface. Hence, it is suggested that apparently adjacent or intersecting nanodots lie in different depth levels. Furthermore, the nanodots do not significantly pierce through the 2 nm thick plasma oxide as presented in Sect. 3.1.

By contacting the top and rear side of the sample, I–V measurements through the Al/c-Si wafer/Si-nanodots/Ag system were carried out recently [35]. The current density was comparable to a plasma oxidized c-Si wafer exhibiting a series resistance of 10 kΩ. This shows that the distance between the nanodots is short enough to allow an electrical transport by tunneling mechanisms which is an important prerequisite for the implementation of the nanodots as an

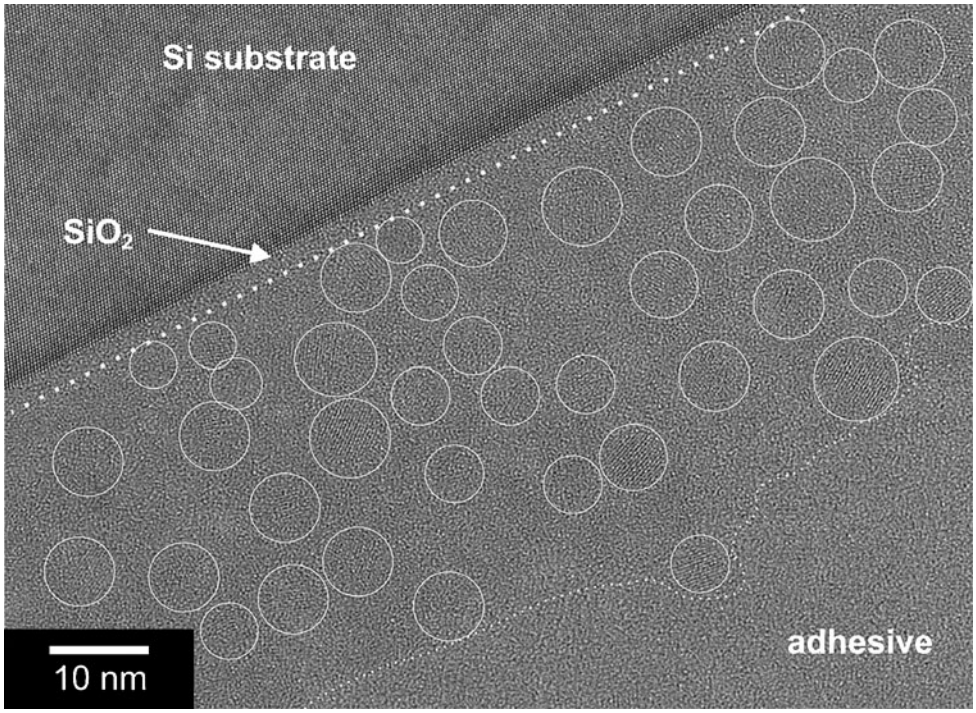

Fig. 4 HRTEM micrograph showing a cross-section of a stack of 8 nanodot layers. A *white guide line* is drawn to mark the upper border of the plasma oxide. The outer borders of the nanodots are marked by *white circular lines*

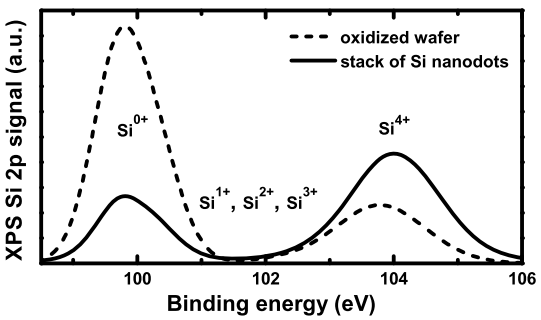

Fig. 5 XPS spectrum of the Si 2p line of a plasma oxidized c-Si wafer and of a stack of 8 nanodot layers. The suboxide fraction for both sample structures is about 6 %

emitter in a solar cell device. Consequently, higher current densities can be achieved by decreasing the oxide thickness [36].

XPS measurements were performed in order to compare the plasma oxidation of the nanodots with the plasma oxidation of the c-Si wafer. Figure 5 shows the Si 2p line of a plasma oxidized Si wafer before and after the growth of the stacked nanodot-layers. The information depth of the XPS system used is about 10 nm. Therefore, a significant contribution of the oxide layer located directly on the substrate to the XPS signal acquired from the stacked nanodots can be excluded.

For both measurements, the spectrum shows two major peaks located at 99.8 eV and 103.8 eV which correspond to nonoxidized silicon atoms (Si^{0+}) and fourfold oxidized silicon atoms (Si^{4+}), respectively [37]. The Si^{4+} signal of the nanodot system is stronger compared to the oxidized wafer due to the multiple oxide layers, whereas the Si^{0+} signal of the oxidized wafer is stronger due to the contribution of the Si wafer. An equally low signal from suboxides (i.e., partially oxidized silicon atoms: Si^{1+}, Si^{2+}, and Si^{3+}) was measured for both samples.

By fitting the XPS spectra with one Gaussian peak per oxidation state and using a Shirley background [38], the fraction of the suboxides was determined to 6 % for both sample structures in Fig. 5. The abruptness of the nanodots separating oxide reveals that a layer by layer oxidation performed by plasma oxidation is also possible for nonplanar surfaces. Hence, the same high passivation quality for the nanodots covered with the plasma oxide as for the plasma oxidized substrate is expected.

For confirmation of this prediction, TRPL spectroscopy was performed in order to obtain the lifetime of photogenerated charge carriers inside of the nanodots. Figure 6 shows the decay of the PL signal at 1100 nm of the stacked nanodot layers and the c-Si wafer substrate acquired by laser excitation at 337 nm and 743 nm, respectively. A strong contribution of the c-Si wafer to the nanodot PL can be excluded since the absorption depth of the excitation wavelength (337 nm) in crystalline silicon is only about 10 nm. Furthermore, the PL decay of the wafer is much faster than for the nanodot system as shown in Fig. 6. By fitting the PL decays with an exponential function [39], the charge carrier lifetime was determined to 18 µs for the nanodot system and to 1 µs for the bulk material. The low lifetime for the bulk

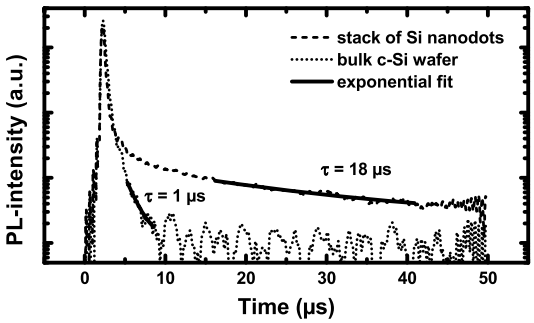

Fig. 6 Photoluminescence decay at 1100 nm of a stack of 8 nanodot layers and the c-Si wafer substrate acquired by laser excitation at 337 nm and 743 nm, respectively. The charge carrier lifetime τ was determined by fitting the decays with an exponential function

material is explained by a high surface recombination velocity at the nonpassivated and rough rear side of the wafer.

In comparison to the charge carrier lifetime of the nanodots, the lifetime in polycrystalline silicon exhibiting 2 orders of magnitude larger grain sizes is only of about 10 ns [40]. This result illustrates the main benefit of the passivating oxide layer surrounding the nanodots and opens up the possibility to use the presented nanodot structures as absorber material in thin film 3rd generation solar cells.

4 Conclusion

Highly crystalline silicon nanodots were grown onto ultrathin oxidized c-Si wafers by combining the dewetting process of thin a-Si layers at UHV conditions and plasma oxidation. Both processes allow the formation of nanodots at lower temperatures than for commonly used nanostructure growth mechanisms. The size, the shape, the density, and the crystallinity of the nanodots are determined by the thickness of the initial a-Si layer. The diameter of the nanodots decreases with decreasing initial layer thickness while the areal density of the nanodots increases. Round, single-crystalline nanodots are grown by 3 nm a-Si layers, where the coalescence of multiple nanodots to polycrystalline nanodots does not occur. A controlled layer-by-layer oxidation of the nanodots is provided by plasma oxidation, as verified by XPS.

The nanostructures presented in this work exhibit promising properties to meet the prerequisites for the application as a nanodot heteroemitter in a solar cell device.

By stacking several nanodot layers and ultrathin oxides, a high nanodot density is achieved. The close nanodot distances allow electrical transport by tunneling. Thinner passivation oxides can further improve the tunneling current. Furthermore, the high crystallinity of the nanostructures improves both the lifetime and the mobility of charge carriers in the nanodots.

A high passivation of the nanodots and the substrate is provided by the plasma oxidation. During nanodot formation, the ultrathin oxide is not penetrated appreciably by the nanostructures so that the passivation quality of the oxide is preserved. The complete coverage of the nanodots with a plasma oxide improves the charge carrier life time inside of the nanodots. In this way, highly passivated, intrinsic nanodots may also be utilized in an absorber material of 3rd generation solar cells.

For the implementation of the nanodots in a solar cell device, doped stacks of nanodots have to be fabricated. The dewetting process of doped layers is currently under investigation.

Finally, in order to exploit quantum size effects, nanodots with a diameter of less than 5 nm have to be synthesized. For this purpose, thinner initial a-Si layers (<1 nm) may be utilized. However, a subsequent, complete oxidation of such nanodots has to be prevented. A second possibility could be the synthesis of nanodots with a diameter of larger than 5 nm with a subsequent oxidation of the outer shell in order to reduce the diameter of the crystalline fraction.

Acknowledgements The authors would like to thank Thomas Lussky, Dagmar Patzek, Kerstin Jacob, and Anja Scheu for sample preparation and technical support. The authors thank the Max Planck Institute of Microstructure Physics Halle for the access to the JEM 4010 microscope. This work was funded by the Bundesministerium für Bildung und Forschung within the joint research project SINOVA (03SF0352) and by the EU project NanoPV (FP7-NMP3-SL-2011-246331).

References

1. G. Conibeer, M. Green, R. Corkish, Y. Cho, E. Cho, C. Jiang, T. Fangsuwannarak, E. Pink, Y. Huang, T. Puzzer, T. Trupke, B. Richards, A. Shalav, K. Lin, Thin Solid Films **511/512**, 654 (2006)
2. L. Tsakalakos, Mater. Sci. Eng., R Rep. **62**, 175 (2008)
3. A.J. Nozik, Nano Lett. **10**, 2735 (2010)
4. P.V. Kamat, J. Phys. Chem. C **112**, 18737 (2008)
5. W. Shockley, H.S. Quiesser, J. Appl. Phys. **32**, 510 (1961)
6. A.A. Cottey, J. Phys. C, Solid State Phys. **4**, 1734 (1971)
7. T. Takagahara, K. Takeda, Phys. Rev. B **46**, 15578 (1992)
8. E. Cho, M.A. Green, G. Conibeer, D. Song, Y. Cho, G. Scardera, S. Huang, S. Park, X. Hao, Y. Huang, L.V. Dao, Adv. Optoelectron. **2007**, 1 (2007)
9. M.A. Green, Prog. Photovolt: Res. Appl. **9**, 123 (2001)
10. A. Le Bris, J.F. Guillemoles, Appl. Phys. Lett. **97**, 113506 (2010)
11. A. Pecora, L. Maiolo, G. Fortunato, C. Caligiore, J. Non-Cryst. Solids **352**, 1430 (2006)
12. E. Yablonovitch, T. Gmitter, IEEE Electron Device Lett. **6**, 597 (1985)
13. E. Yablonovitch, T. Gmitter, R.M. Swanson, Y.H. Kwark, Appl. Phys. Lett. **47**, 1211 (1985)
14. A. Ghetti, Microelectron. Eng. **59**, 127 (2001)
15. M. Zacharias, J. Heitmann, R. Scholz, U. Kahler, M. Schmidt, J. Bläsing, Appl. Phys. Lett. **80**, 661 (2002)
16. E. Cho, S. Park, X. Hao, D. Song, G. Conibeer, S. Park, M.A. Green, Nanotechnology **19**, 245201 (2008)

17. I. Perez-Wurfl, X. Hao, A. Gentle, D. Kim, G. Conibeer, M.A. Green, Appl. Phys. Lett. **95**, 153506 (2009)
18. T. Matsuyama, K. Wakisaka, M. Kameda, M. Tanaka, T. Matsuoka, S. Tsuda, S. Nakano, Y. Kishi, Y. Kuwano, Jpn. J. Appl. Phys. **29**, 2327 (1990)
19. E. Malguth, M. Roczen, O. Gref, A. Schoepke, M. Schmidt, Phys. Status Solidi A **208**, 612 (2010)
20. Y. Wakayama, T. Tagami, S. Tanaka, Thin Solid Films **350**, 300 (1999)
21. D.T. Danielson, D.K. Sparacin, J. Michel L.C. Kimerling, J. Appl. Phys. **100**, 083507 (2006)
22. B. Yang, P. Zhang, D.E. Savage, M.G. Lagally, Phys. Rev. B **72**, 235413 (2005)
23. P. Sutter, W. Ernst, Y.S. Choi, E. Sutter, Appl. Phys. Lett. **88**, 141924 (2006)
24. B. Legrand, V. Agache, J.P. Nys, V. Senez, D. Stievenard, Appl. Phys. Lett. **76**, 3271 (2000)
25. B. Legrand, V. Agache, T. Mélin, J.P. Nys, V. Senez, J. Appl. Phys. **91**, 106 (2002)
26. H. Angermann, W. Henrion, M. Rebien, D. Fischer, J.T. Zettler, A. Röseler, Thin Solid Films **313/314**, 552 (1998)
27. B. Stegemann, D. Sixtensson, T. Lussky, U. Bloeck, M. Schmidt, CHIMIA Int. J. Chem. **61**, 826 (2007)
28. B. Stegemann, D. Sixtensson, T. Lussky, A. Schoepke, I. Didschuns, B. Rech, M. Schmidt, Nanotechnology **19**, 424020 (2008)
29. K.J. Kim, K.T. Park, J.W. Lee, Thin Solid Films **500**, 356 (2006)
30. P. Temple, C. Hathaway, Phys. Rev. B **7**, 3685 (1973)
31. L. Zhen-Kun, K. Yi-Lan, H. Ming, Q. Yu, X. Han, N. Hong-Pan, Chin. Phys. Lett. **21**, 403 (2004)
32. G. Morel, R.S. Katiyar, S.Z. Weisz, H. Jia, J. Shinar, I. Balberg, J. Appl. Phys. **78**, 5120 (1995)
33. C. Smit, R.A.C.M.M. van Swaaijb, H. Donker, A.M.H.N. Petit, W.M.M. Kessels, M.C.M. van de Sanden, J. Appl. Phys. **94**, 3582 (2003)
34. M. Morita, T. Ohmi, E. Hasegawa, M. Kawakami, M. Ohwada, J. Appl. Phys. **68**, 1272 (1990)
35. M. Roczen, E. Malguth, M. Schade, A. Schöpke, O. Gref, T. Barthel, J.A. Töfflinger, M. Schmidt, H.S. Leipner, L. Korte, B. Rech, J. Non-Cryst. Solids (2011). doi:10.1016/j.jnoncrysol.2011.11.024
36. B. Stegemann, L. Korte, O. Gref, T. Lussky, M. Schmidt, H. Angermann, in *Proceedings of the 26th EUPVSEC* (2011). doi:10.4229/26thEUPVSEC2011-2BV.3.8
37. S. Lombardo, S.U. Campisano, Mater. Sci. Eng., R Rep. **17**, 281 (1996)
38. D.A. Shirley, Phys. Rev. B **5**, 4709 (1972)
39. V.Y. Timoshenko, A.B. Petrenko, M.N. Stolyarov, T. Dittrich, W. Fuessel, J. Rappich, J. Appl. Phys. **85**, 4171 (1999)
40. J. Wong, J.L. Huang, B. Eggleston, M.A. Green, O. Kunz, R. Evans, M. Keevers, R.J. Egan, J. Appl. Phys. **107**, 123705 (2010)